NeuroImage 271 (2023) 120046

Contents lists available at ScienceDirect

NeuroImage

journal homepage: www.elsevier.com/locate/neuroimage

Reliability of spinal cord measures based on synthetic T_1-weighted MRI derived from multiparametric mapping (MPM)

Simon Schading[a,1], Maryam Seif[a,b,1], Tobias Leutritz[b], Markus Hupp[a], Armin Curt[a], Nikolaus Weiskopf[b,c], Patrick Freund[a,b,d,*]

[a] Spinal Cord Injury Center, Balgrist University Hospital, University of Zurich, Forchstrasse 340, Zurich 8008, Switzerland
[b] Department of Neurophysics, Max Planck Institute for Human Cognitive and Brain Sciences, Leipzig, Germany
[c] Felix Bloch Institute for Solid State Physics, Faculty of Physics and Earth Sciences, Leipzig University, Leipzig, Germany
[d] Wellcome Trust Centre for Neuroimaging, UCL Queen Square Institute of Neurology, University College London, United Kingdom of Great Britain and Northern Ireland, London, UK

ARTICLE INFO

Keywords:
Synthetic T_1-weighted MRI
Quantitative MRI
Neurodegeneration
Spinal cord injury
Cervical cord atrophy

ABSTRACT

Short MRI acquisition time, high signal-to-noise ratio, and high reliability are crucial for image quality when scanning healthy volunteers and patients. Cross-sectional cervical cord area (CSA) has been suggested as a marker of neurodegeneration and potential outcome measure in clinical trials and is conventionally measured on T_1-weigthed 3D Magnetization Prepared Rapid Acquisition Gradient-Echo (MPRAGE) images. This study aims to reduce the acquisition time for the comprehensive assessment of the spinal cord, which is typically based on MPRAGE for morphometry and multi-parameter mapping (MPM) for microstructure. The MPRAGE is replaced by a synthetic T_1-w MRI (synT_1-w) estimated from the MPM, in order to measure CSA. SynT_1-w images were reconstructed using the MPRAGE signal equation based on quantitative maps of proton density (PD), longitudinal (R_1) and effective transverse (R_2^*) relaxation rates. The reliability of CSA measurements from synT_1-w images was determined within a multi-center test-retest study format and validated against acquired MPRAGE scans by assessing the agreement between both methods. The response to pathological changes was tested by longitudinally measuring spinal cord atrophy following spinal cord injury (SCI) for synT_1-w and MPRAGE using linear mixed effect models. CSA measurements based on the synT_1-w MRI showed high intra-site (Coefficient of variation [CoV]: 1.43% to 2.71%) and inter-site repeatability (CoV: 2.90% to 5.76%), and only a minor deviation of -1.65 mm^2 compared to MPRAGE. Crucially, by assessing atrophy rates and by comparing SCI patients with healthy controls longitudinally, differences between synT_1-w and MPRAGE were negligible. These results demonstrate that reliable estimates of CSA can be obtained from synT_1-w images, thereby reducing scan time significantly.

Abbreviations

CNR	Contrast-to-noise ratio
CoV	Coefficient of variation
CSA	Cross-sectional spinal cord area
FoV	Field of view
MPM	Multi-parameter mapping
MPRAGE	T_1-weighted 3D Magnetization Prepared Rapid Acquisition Gradient-Echo
SCI	Spinal cord injury
synT_1-w MRI	Synthetic T_1-weighted MRI
THS	Traveling heads study
VL	Vertebral level

1. Introduction

One of the most common magnetic resonance imaging (MRI) modalities is T_1-weighted (T_1-w) MRI which is routinely applied in the clinics and research to assess tissue structures and determine volumetric changes in the brain and spinal cord. For instance, spinal cord geometry measures such as the cross-sectional area (CSA) can be determined on T_1-w images (Chien et al., 2020; Cohen-Adad et al., 2021; Freund et al., 2010; Lundell et al., 2011). Measuring the CSA has been suggested as a marker for pathologic effects in different diseases such as spinal cord injury (SCI) and multiple sclerosis, and as a potential outcome measure in clinical trials for which reliable MRI protocols are required (Casserly et al., 2018; Freund et al., 2013a; Kearney et al., 2015;

* Corresponding author at: Spinal Cord Injury Center, Balgrist University Hospital, University of Zurich, Forchstrasse 340, Zurich 8008, Switzerland.
E-mail address: patrick.freund@balgrist.ch (P. Freund).
[1] shared first authors

https://doi.org/10.1016/j.neuroimage.2023.120046.
Received 6 January 2023; Received in revised form 14 March 2023; Accepted 18 March 2023
Available online 21 March 2023.

Schmierer and Miquel, 2018; Seif et al., 2019). Routinely, a high resolution (1 mm^3 isotropic) T_1-w 3D Magnetization Prepared Rapid Acquisition Gradient-Echo (MPRAGE) sequence is used with an acquisition time of 10 min depending on the volume of interest.

MRI scans with a short acquisition time, high signal-to-noise and contrast-to-noise ratios (CNR) are desirable when measuring patients in the MR scanner. Long acquisition time often leads to increased patient's discomfort and motion which in turn can result to motion artifacts (Oztek et al., 2020). Synthetic MRI is a technique that enables to reconstruct multiple contrast weighted images based on quantitative maps of physical tissue properties (Nöth et al., 2015; Tanenbaum et al., 2017). It has already been shown that synthetic MRI may provide a valid alternative to conventional MR acquisitions in the brain for assessing its morphology and generating diagnostic images in several diseases such as brain tumors, epilepsy, and multiple sclerosis (Gracien et al., 2019; Granberg et al., 2016; Nöth et al., 2015). Thus, this approach helps us to generate several contrast weightings from the same acquisition and thereby shorten the acquisition time, which is beneficial for both clinical routine and long study protocols. For the reconstruction of synthetic MR images quantitative MRI protocols are required. The multi-parameter mapping (MPM) protocol (Helms et al., 2008; Weiskopf et al., 2013) is a quantitative MRI protocol and provides quantitative maps of proton density (PD), magnetization saturation, and longitudinal (R_1) and effective transverse ($R_2{}^*$) relaxation rates. These quantitative maps are sensitive to the tissue microstructure such as myelin and iron content and are used as surrogate markers in neuroimaging studies (Weiskopf et al., 2021). Crucially, they allow the reconstruction of a synthetic T_1-weighted (synT_1-w) image, which can be used for morphological assessments such as the CSA. Therefore, using only the MPM protocol for quantitative maps and the resulting synthetic T_1-w MRI may allow us to reduce the total scan time as the acquisition of an additional conventional structural T_1-w image would not be necessary.

However, the implementation of this new outcome measure in clinical studies, in particular when conducting multi-center studies, requires high reliability and validity, which are still unknown for measuring the CSA on synT_1-w images.

Here, we (1) reconstructed synthetic T_1-w images based on quantitative maps derived from the MPM protocol of the cervical spinal cord, (2) explored the test-retest repeatability of the spinal cord cross-sectional area measurements from C1 to C3 in a multi-center study, and (3) validated the application of the generated synT_1-w images in a longitudinal study to reliably detect cord atrophy in patients suffering from spinal cord injury by comparing the synT_1-w MRI against the reference standard MPRAGE.

2. Materials and methods

2.1. Participants and study design

This study includes two different MRI data sets acquired within our previous studies, a: The "Traveling heads study (THS)" (Leutritz et al., 2020; Seif et al., 2022) for assessing intra- and inter-site repeatability, and b: a longitudinal dataset (Freund et al., 2013b) of SCI patients and healthy controls to test how the approach of reconstructing synthetic T_1-w images and measuring changes in spinal cord area generalizes to a patient group.

The THS included 5 healthy volunteers (male (m)/female (f): 3/2, age: 32.4 ± 6.0 years) who underwent the MPM protocol twice (i.e. scan-rescan) at 6 different sites with an average inter-scan interval of 2 h between scan-rescan measurements at each site. See Table 1 for an overview of the 6 different sites where the data were acquired.

The longitudinal study aims at tracking changes of morphological metrics derived from structural MR imaging and compares the established reference standard (MPRAGE) with the synT_1-w MRI. 23 patients with acute SCI (m/f: 17/6, age [mean ± SD]: 46.8 ± 19.2 years, admission to the Balgrist University Hospital between September 2010 and August 2014), as well as 21 healthy controls (m/f: 13/8, age [mean ± SD]: 33.7 ± 9.8 years) were scanned at 5 different time points (at baseline, 2 months, 6 months, 1 year, and 2 year follow-up) over a time period of 2 years following enrollment/SCI. There was a significant difference in mean age between healthy controls and SCI patients ($p = 0.017$, Wilcoxon rank-sum test), while no sex imbalance was evident ($p = 0.52$, Fisher's exact test). Traumatic ($n = 15$) and non-traumatic ($n = 8$) etiologies of SCI were included in the patient cohort. The initial neurological level of injury ranged from C3 to T11 (13 tetraplegics, 10 paraplegics). Eight SCI patients were classified based on the American Spinal Injury Association Impairment Scale (AIS) as AIS A, 5 SCI patients as AIS B, 3 SCI patients as AIS C, and 7 SCI patients as AIS D. Detailed demographic and clinical information of SCI patients is listed in Table 2.

2.2. Ethics statement

The five subjects participating in the THS provided written informed consent before each scan and every site obtained approval by the local ethics committees. All participants of the longitudinal study also provided written informed consent before participating in the study, which was approved by the local Ethics Committee of Zurich (EK-2010–0271).

2.3. Image acquisition

In the THS, subjects underwent a quantitative imaging protocol on 3T MRI systems (Table 1), based on the MPM protocol (Weiskopf et al., 2013), that was implemented using product sequences available on each clinical MRI system (Leutritz et al., 2020; Seif et al., 2022). The field of view (FoV) covered the brain and cervical levels C1-C5. The MPM protocol consisted of three 3D multi-echo spoiled gradient-echo sequences (i.e. fast low-angle shot (FLASH) on Siemens scanners, and multi-echo fast field echo (mFFE) on Philips scanners), each with distinct parameters for T_1-, proton-density (PD)-, and magnetization-transfer (MT)-weighting: repetition time (TR) of PD- and T_1-weighted contrasts: 18 ms; excitation flip angles for MT-, PD- and T_1-weighted contrasts: 6°, 4°, 25°, respectively. Commonly shared settings across all modalities were: six equidistant echoes, 1 mm^3 isotropic reconstruction voxel size; readout FoV: 256 mm; base resolution: 256 pixels in the readout direction; 176 slices; readout in the head-foot direction, inner phase encoding loop in the left-right ("slice", fast phase encoding) direction, outer phase encoding loop in the anterior-posterior direction ("phase", slow phase encoding); readout bandwidth: 480 Hz/pixel; elliptical k-space coverage; parallel imaging speedup factor of 2 in the slow/slice phase encoding direction. The scanning parameters that differed between scanner types are listed in Table 3. Total scan time on Siemens scanners was 18:45 min and on Philips scanners 23:58 min. For more details please refer to (Leutritz et al., 2020).

In the longitudinal study subjects (SCI patients and healthy controls) were scanned with a T_1-weighted 3D Magnetization Prepared Rapid Acquisition Gradient-Echo (MPRAGE) sequence as well as the MPM protocol on clinical 3T scanners (Siemens Verio and Siemens Skyra, Erlangen, Germany), both covering the brain and cervical levels C1-C5. The MPRAGE sequence had the following parameters: 176 slices, in-plane FoV: 224 × 256 mm^2, 1 mm^3 isotropic resolution, TR = 2420 ms, TE = 4.28 ms, flip angle = 9°, inversion time (TI) = 960 ms, readout bandwidth: 150 Hz/pixel, total scan time: 9:04 min. The MPM protocol used in the longitudinal study was similar to the protocol used in the THS except for $B_1{}^+/B_1{}^-$ mapping, which was not performed. It was implemented using product sequences available on the respective MRI scanner (Leutritz et al., 2020). The following parameters were used: 176 slices, FoV: 240 × 256 mm^2, 1 mm^3 isotropic resolution, parallel imaging (GRAPPA) with a speedup factor of 2, and readout bandwidth: 480 Hz/pixel. TR of PD- and T_1-weighted contrasts was 25 ms, while the

Table 1
MRI scanning sites, the respective MRI systems, and main hardware/software specifications.

Site	MRI vendor	MRI system	No. of channels of RF receive head coil	MRI software version
BCN	Siemens	Verio	32	VD13A
BSL	Siemens	Prisma	20	VE11C
HD	Siemens	Verio	16	VB19A
NOT	Philips	Achieva	16	5.3.0
SNS	Philips	Achieva	16	5.2.7
ZH	Siemens	Skyra	16	VE11B

BCN Clinica Creu Blanca, Barcelona, Spain; *BSL* Radiology Department, University Hospital Basel, Basel, Switzerland; *HD* University Hospital Heidelberg, Heidelberg, Germany; *NOT* Radiology, Swiss Paraplegic Center, Nottwil, Switzerland; *SNS* Laboratory for Social and Neural Systems Research, Zurich Center for Neuroeconomics, University of Zurich, Zurich, Switzerland; *ZH* Spinal Cord Injury Center, Balgrist University Hospital, Zurich, Switzerland.

Table 2
Demographic and clinical information of SCI patients.

Age at injury (years)	Sex	Initial AIS	Initial neurological level of injury	Level of hyperintensive signal change	Injury mechanism
18	M	A	C5	C5-C7	Burst fracture C6
46	F	D	T8	T6-T12	Prolapsed disc T8/9 with spinal cord ischemia
22	M	B	C7	C6/7	Dislocation fracture C6/7
67	F	B	T9	T6-T12	AV-fistula T9-T11 with myelopathy
77	F	D	T10	T9-conus medullaris	Aortic embolism with spinal cord ischemia
43	M	D	T11	None	Massively prolapsed disc L3/4
41	M	A	C5	C6/7	Anterolisthesis of C6 relative to C7
70	M	B	C7	C7	Hyperflexion C6/7
20	M	A	C5	C5/6	Dislocation fracture C5/6
52	M	D	T9	– [a]	Flexion-distraction T9/10
30	M	B	C7	C6/7	Dislocation fracture C6/7
29	M	A	T11	– [a]	Flexion-distraction T12/L1 & burst fracture L1
47	M	D	C4	C6/7	Dislocation fracture C6/7
51	M	B	C6	C6/7	Dislocation fracture C6/7
67	M	D	C3	C3/4	Spinal cord compression C3/4 & acute contusion
71	M	C	T10	T10–12	Spinal cord ischemia
32	M	A	C5	C6/7	Flexion-distraction C5-C7
53	F	C	C4	C4/5	Spinal cord compression C4/5
71	F	D	T3	T6-T8	Discogenic spinal cord compression T3-T9
72	F	A	T11	T10-T12	Spinal epidural hematoma
30	M	A	C4	C5/6	Dislocation fracture C5/6 & burst fracture C6
28	M	A	C4	C4/5	Dislocation fracture C4/5
31	M	C	T2	T2-T7	Dislocation fracture T4/5

[a] Spinal cord cannot be assessed at the level of injury due to artifacts caused by metal implants*AIS* American Spinal Injury Association Impairment Scale.

Table 3
Differing scanning parameters of Siemens and Philips systems.

Acquisition parameter	Siemens	Philips
Minimum TE and echo spacing (ms)	2.46	2.40
Acquisition resolution (mm^3)	1.1 × 1.0 × 1.1	1.0 × 1.0 × 1.0
FoV slice resolution (%)	91.0	78.5
FoV phase (%)	87.50	93.75
Slice partial Fourier (%)	75.0	62.5
Phase parallel speedup factor	2	2
Slice parallel speedup factor	1.00	1.25
Spoiling phase increment (°)	50	150
MT TR (ms)	37	48
MT pulse flip angle (°)	500	220
MT pulse length (ms)	10	8
MT pulse off-resonance frequency (kHz)	1.2	1.0
MT pulse shape	Gaussian	Gaussian filtered sinc
MT pulse bandwidth (Hz)	192	300

TE echo time, *FoV* field of view, *MT* magnetization transfer, *TR* repetition time.

MT-weighted contrast had a TR of 37 ms. Flip angles for PD-, T_1-, and MT-weighted contrasts were 4°, 23°, 9° respectively. Six (MT-weighted) and eight (PD- and T_1-weighted) echoes with equidistant echo spacing of 2.46 ms and the first TE being 2.46 ms were acquired. The off-resonance RF pulse for MT-weighting had the same properties as listed for the Siemens scanner in Table 3. The total scan time was 23 min.

2.4. Synthetic T_1-w MRI calculation

PD, R_1, and R_2^* maps were generated based on the T_1-weighted, PD-weighted, and MT-weighted images from the MPM protocol using the SPM12-based (v7487) hMRI toolbox (v0.2.0) (Leutritz et al., 2020; Tabelow et al., 2019). First, all images with different echoes were co-registered to account for possible subject motion. In the THS the maps were estimated from the multi-echo data in combination with the B_1^+ and B_1^- measurements. For PD and R_1 the estimation was based on the rational approximation of the signal (Helms et al., 2008) with additional corrections for B_1^+ inhomogeneities. R_2^* was calculated across all contrasts (PD-w, T_1-w, MT-w) using the ESTATICS approach (Weiskopf et al., 2014). Extrapolation of the signal to TE = 0 reduced R_2^*-related bias in PD maps and was combined with estimations of B_1^- sensitivity for further bias reduction of the PD maps (Leutritz et al., 2020; Seif et al., 2022). In the longitudinal SCI study, the maps were calculated likewise. However, since B_1^+ maps were not recorded in the longitudinal study, the RF transmit field B_1^+ inhomogeneities were corrected using the post-processing UNICORT correction (Weiskopf et al., 2011) as available in the hMRI toolbox (Tabelow et al., 2019) without correction for imperfect RF spoiling.

SynT_1-w images were calculated using in-house MATLAB scripts (Version 9.7.0.1190202 (R2019b)) based on quantitative maps of PD, R_1, and R_2^* using the MPRAGE signal equation for calculating the signal intensity (S) without undesired B_1^+/B_1^- effects assuming linear k-space

sampling with centered main echo (Deichmann et al., 2000; Nöth et al., 2015):

$$S = PD \cdot \sin(\alpha) \cdot \exp\left(-TE \cdot R_2^*\right) \cdot Q \tag{1}$$

Where Q is given by:

$$\frac{E_4 \cdot (1 - 2 \cdot E_1 + E_1 \cdot E_2) + T_1^* \cdot R_1 \cdot (1 + E_1 \cdot E_2 \cdot E_3 - E_1 \cdot E_2 \cdot E_4 - E_4)}{1 + E_1 \cdot E_2 \cdot E_3} \tag{2}$$

With the parameters:

$$T_1^* = \left(R_1 - \frac{1}{ES} \cdot \ln(\cos(\alpha))\right)^{-1} \tag{3}$$

$$E_1 = \exp\left(-\left(TI - \frac{\tau}{2}\right) \cdot R_1\right) \tag{4}$$

$$E_2 = \exp\left(-TD \cdot R_1\right) \tag{5}$$

$$E_3 = \exp\left(-\frac{\tau}{T_1^*}\right) \tag{6}$$

$$E_4 = \exp\left(-\frac{\tau}{2 \cdot T_1^*}\right) \tag{7}$$

Where α = flip angle, TE = echo time, TR = repetition time, TI = inversion time, ES = echo spacing, TD = delay time, and τ = readout duration of the reconstructed synT$_1$-w image. TD and τ can be derived as follows:

$$\tau = n \cdot ES \tag{8}$$

$$TD = TR - \left(TI - \frac{\tau}{2}\right) - \tau \tag{9}$$

Where n denotes the number of sagittal partitions of the simulated MPRAGE acquisition.

Fig. 1 shows a representative example of a synT$_1$-w image and illustrates the calculation process.

2.5. Optimization of sequence parameters (THS data)

The sequence parameters were first optimized to achieve the maximum CNR between the spinal cord and the surrounding cerebrospinal fluid (CSF) allowing for better segmentation of the spinal cord (Gros et al., 2019).

Binary masks of the spinal cord and CSF for the calculation of the CNR within these regions were obtained using the Spinal Cord Toolbox (Version 5.5) (De Leener et al., 2017). The segmentations were performed on synT$_1$-w images that had been calculated with the following parameters according to (Tardif et al., 2009): (α = 9°, TE = 4.19 ms, TR = 2420 ms, TI = 960 ms, ES = 9.9 ms). First, the spinal cord was automatically segmented applying the *sct_deepseg_sc* algorithm (Gros et al., 2019), while the *sct_propseg* algorithm (De Leener et al., 2014) provided segmentations of the vertebral canal (sum of CSF and spinal cord). All resulting binary masks were visually inspected and manually corrected if necessary. The spinal cord segmentation was subtracted from the vertebral canal segmentation in order to obtain the CSF segmentation only. Both segmentations were visually inspected and manually corrected where necessary. The synT$_1$-w image was co-registered to the MNI-Poly-AMU template (De Leener et al., 2018) after semiautomatic identification of vertebral levels C1-C3. Finally, the average voxel intensities within the spinal cord (μ_{cord}) and CSF (μ_{CSF}) segmentations as well as the standard deviation of the voxel intensities within the spinal cord (σ_{cord}) segmentation were extracted at vertebral levels C1-C3, respectively.

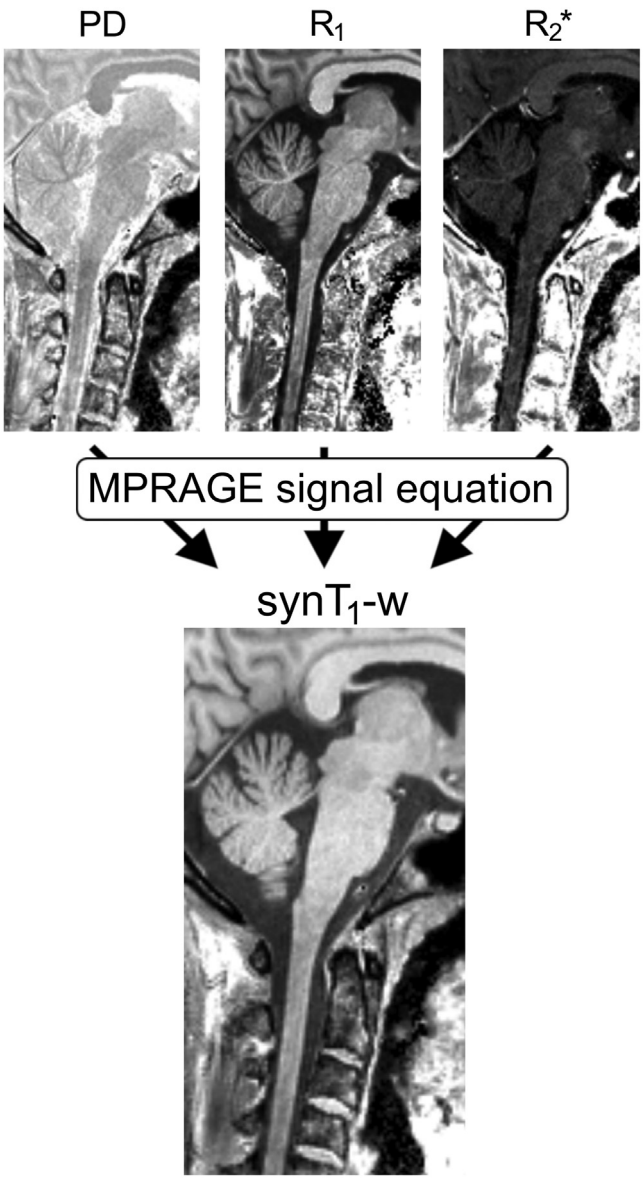

Fig. 1. Illustration of reconstruction of the synT$_1$-w image. Based on the quantitative maps derived from the multi-parametric mapping protocol and using the MPRAGE signal equation, a synthetic T$_1$-w image was calculated and reconstructed.

The CNR was defined as follows:

$$CNR = \frac{\mu_{cord} - \mu_{CSF}}{\sigma_{cord}} \tag{10}$$

Where μ_{cord} and μ_{CSF} denote the mean signal within the spinal cord and CSF segmentations, and σ_{cord} the standard deviation of the signal within the spinal cord, respectively.

The following parameters were optimized within the reported limits close to frequently used settings of MPRAGE acquisitions (Tardif et al., 2009) using a simple grid search: α = 9–13°, TE = 4.2–4.5 ms, TR = 2100–2700 ms, TI = 940–980 ms, ES = 9.9 ms, and n = 176 partitions. For each of the combinations the CNR was calculated and the optimal sequence parameters were determined according to the highest resulting CNR across all subjects and sites for allowing robust spinal cord segmentation (Gros et al., 2019).

2.6. Image processing and spinal cord segmentation

For obtaining the CSA, synT$_1$-w and MPRAGE images were automatically segmented using the *sct_deepseg_sc* algorithm within the Spinal Cord Toolbox (Gros et al., 2019) and the resulting binary masks were manually corrected if necessary. Following segmentation, synT$_1$-w and MPRAGE images were co-registered to the MNI-Poly-AMU template (De Leener et al., 2018) after semiautomatic identification of different vertebral levels (C1–C3), and the average CSA was extracted from the segmentations for each vertebral level (C1–C3) separately.

2.7. Intra- and inter-site repeatability (THS data)

Intra-site (i.e. scan-rescan) and inter-site repeatability of the spinal cord segmentation was assessed by calculating coefficients of variation (CoV) for CSA across vertebral levels (VL) C1-C3.

For assessing the intra-site repeatability, an intra-site CoV was defined as the standard deviation (σ_{intra}) of scan-rescan measurements of each subject per site over the mean (μ_{intra}) of scan-rescan measurements of each subject per site:

$$CoV_{intra}(VL, site, subject) = \frac{\sigma_{intra}}{\mu_{intra}} \cdot 100 \quad (11)$$

The intra-site CoV was calculated for each vertebral level, site, and subject separately.

For comparing the repeatability between sites, the inter-site CoV was defined as the standard deviation (σ_{inter}) of all measurements of each subject across all sites over the mean (μ_{inter}) of all measurements of each subject across all sites:

$$CoV_{inter}(VL, subject) = \frac{\sigma_{inter}}{\mu_{inter}} \cdot 100 \quad (12)$$

The inter-site CoV was calculated for each vertebral level and subject separately.

Further statistical analyses were performed in RStudio (Version 4.0.5).

2.8. Agreement between CSA from MPRAGE and synT$_1$-w (Longitudinal data)

Next, the difference between CSA obtained from synT$_1$-w and the reference standard MPRAGE was further assessed using the Bland-Altman method (Bland and Altman, 1986), where the difference between both segmentations (MPRAGE and synT$_1$-w) was plotted against their average for each data point. A data point denotes the parameter CSA of one subject at one time point averaged across vertebral levels C1-C3. The bias, which represents the average of the individual differences between MPRAGE and synT$_1$-w, and the limits of agreement, encompassing 95% of the individual differences between MPRAGE and synT$_1$-w, were determined across vertebral levels C1-C3.

2.9. Tracking SCI-induced cord atrophy using MPRAGE and synT$_1$-w (Longitudinal data)

The image quality of both MPRAGE and synT$_1$-w images was carefully inspected and the respective vertebral levels were excluded in case of extensive susceptibility and/or motion artifacts. The final sample size was 85.3% (C1), 82.7% (C2), and 75.4% (C3) of the total sample size. 10.3% of the data was rejected based on the quality assessment of MPRAGE images and 13.6% based on synT$_1$-w images. In the final data set the sex distribution (m/f) in SCI patients was 15/6 and in healthy controls 13/8. Using linear mixed effect models, temporal changes of CSA (i.e. spinal cord atrophy) over two years following SCI across the cervical cord were assessed. The same models were created for both MPRAGE and synT$_1$-w readouts and included vertebral levels (3 levels: C1-C3), time since injury (5 time points) with a quadratic term to model deceleration effects, as well as their interaction with group (2 groups: healthy controls and SCI patients) as fixed effects. Random effects were the individual intercept and slope associated with time since injury and vertebral level, and the quadratic term of time since injury. Moreover, since healthy controls and SCI patients differed with regard to mean age, the interaction of age with time since injury was added to account for aging-related changes (Papinutto et al., 2020). Due to the scanner update over the course of the study, the models were additionally corrected for the scanner type. The linear effects over time (i.e. linear atrophy rates), the quadratic effects (i.e. deceleration), as well as the mean estimated CSA across C1-C3 at baseline and the 2-year follow-up were assessed for both groups and compared between MPRAGE and synT$_1$-w. Similarly, the difference between healthy controls and SCI patients was compared between MPRAGE and synT$_1$-w for the linear effects over time, the quadratic effects, as well as the estimated CSA at baseline and the 2-year follow-up. A significance threshold of $p = 0.05$ and Tukey's correction for multiple comparison was used.

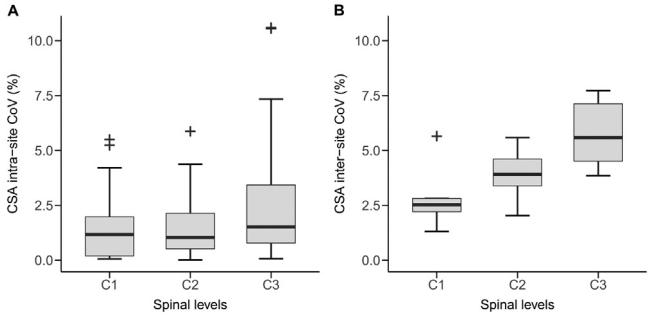

Fig. 2. Spinal cord cross-sectional area (CSA) measurements based on the synT$_1$-w MRI: intra-site coefficient of variation (A) and inter-site coefficient of variation (B) of CSA estimates at cervical levels C1-C3.

3. Results

3.1. Optimization of sequence parameters (THS data)

The CNR was determined on synT$_1$-w images with different sequence parameters (α = 9–13°, TE = 4.2–4.5 ms, TR = 2100–2700 ms, TI = 940–980 ms). The highest CNR was obtained for α = 12°, TE = 4.5 ms, TR = 2100 ms, and TI = 980 ms. Therefore, these MR parameters were applied for creating the synT$_1$-w images for the subsequent analyses. Please note that the optimum within the predefined range of settings was found at the boundary for several parameters.

3.2. Intra- and inter-site repeatability (THS data)

The average intra-site CoV (scan-rescan) for CSA obtained from synT$_1$-w images was 1.43 ± 1.51% for C1, 1.55 ± 1.42% for C2, and 2.71 ± 3.00% for C3 (Fig. 2A) demonstrating high test-retest repeatability. The average inter-site CoV (between different sites) for CSA obtained from synT$_1$-w images was 2.90 ± 1.64% for C1, 3.91 ± 1.33% for C2, and 5.76 ± 1.66% for C3 (Fig. 2B) indicating good repeatability between sites with different MRI systems.

3.3. Agreement between CSA from MPRAGE and synT$_1$-w (Longitudinal data)

The average CSA based on MPRAGE segmentations from the longitudinal data was 63.81 ± 8.69 mm^2 while the mean CSA for synT$_1$-w was 62.19 ± 8.35 mm^2 (Fig. 3A). Fig. 3B shows the Bland-Altman plots for the difference between the CSA obtained from MPRAGE and synT$_1$-w images. Based on the Bland-Altman analysis, the bias of CSA derived from synT$_1$-w was -1.61 mm^2 (-2.5%) compared to MPRAGE with a lower limit of agreement of -5.67 mm^2 (-8.9%) and an upper limit

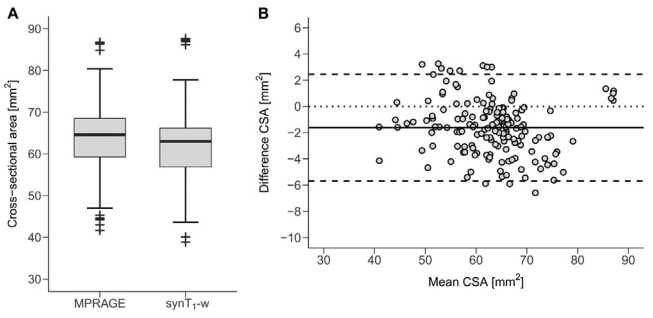

Fig. 3. Average spinal cord cross-sectional area (CSA) across C1-C3 for MPRAGE and synT$_1$-w (A). Bland-Altman plot illustrating the difference between CSA derived from MPRAGE and synT$_1$-w (B).

of agreement of 2.45 mm^2 (3.8%) indicating good agreement between both methods.

3.4. Tracking SCI-induced cord atrophy using MPRAGE and synT$_1$-w MRI (Longitudinal data)

The linear mixed effect models for tracking atrophy across C1-C3 based on MPRAGE and synT$_1$-w segmentations are depicted in Fig. 4A. There was a general offset effect with a lower CSA-intercept observable in the model based on synT$_1$-w compared to that based on MPRAGE in both healthy controls and SCI patients due to smaller segmentations of synT$_1$-w images (compare previous Section 3.3.). Importantly, this offset in CSA between both models (MPRAGE and synT$_1$-w) was comparable between healthy controls (-1.58 mm^2 [-2.4%]) and patients (-1.53 mm^2 [-2.3%]). This offset is in the range of the bias in the Bland-Altman analysis.

The linear atrophy rates and quadratic effects of the linear mixed effect models are reported in Table 4. Overall, MPRAGE and synT$_1$-w showed similar estimates for both healthy controls and SCI patients as well as similar estimates of group differences (Fig. 4B). Both models detected significantly higher linear atrophy rates for CSA (MPRAGE: -0.537 mm^2/month, p = 0.0005; synT$_1$-w: -0.574 mm^2/month, p < 0.0001) in SCI patients compared to healthy controls with similar magnitudes. Likewise, the quadratic effects of both models were comparable for healthy controls, SCI patients and the difference between controls and patients (Fig. 4C).

The average CSA across both groups as well as the difference between both groups at baseline and the 2-year follow-up are reported in Table 5. While the calculated CSA based on the synT$_1$-w were systematically lower for both healthy controls and SCI patients, this bias diminished when assessing differences between groups (Fig. 5). Both the model based on MPRAGE and the model based on T$_1$-w image segmentation showed no significant differences in CSA between healthy controls and SCI patients at baseline (MPRAGE: -1.28 mm^2, p = 0.59; synT$_1$-w: -1.29 mm^2, p = 0.53). However, at the 2-year follow-up both models detected significant reductions of the CSA (MPRAGE: -11.16 mm^2, p = 0.0002; synT$_1$-w: -11.85 mm^2, p = 0.0001) in SCI patients compared to controls with similar magnitudes.

4. Discussion

This study shows the feasibility of reconstructing T$_1$-w synthetic MRI images based on quantitative maps of physical tissue parameters for reliable estimation of spinal cord morphometric parameters such as the cross-sectional area. We demonstrated high intra- and inter-site repeatability of CSA measurements derived from synT$_1$-w images (intra-site CoV < 3%, inter-site CoV < 6%), which opens the opportunity of applying this technique in multi-center studies. The direct comparison of CSA measurements between synT$_1$-w and the reference standard MPRAGE

Table 4
Linear rates and quadratic effects of cross-sectional cord area atrophy averaged across C1-C3 for MPRAGE and synT$_1$-w estimated from linear mixed effects models.

	Cross-sectional area linear rate											
	Controls				Patients				Patients - Controls				
Protocol	Rate [mm^2/month]	95% CI [mm^2/month]			Rate [mm^2/month]	95% CI [mm^2/month]			Rate [mm^2/month]	95% CI [mm^2/month]			p-value
MPRAGE	0.042	−0.215	to	0.300	−0.508	−0.787	to	−0.229	−0.550	−0.930	to	−0.170	0.005
synT$_1$-w	0.041	−0.125	to	0.207	−0.550	−0.742	to	−0.359	−0.591	−0.848	to	−0.335	<0.0001
Difference	−0.001				−0.043				−0.041				

	Cross-sectional area quadratic effect											
	Controls				Patients				Patient - Controls				
Protocol	Rate [mm^2/month^2]	95% CI [mm^2/month^2]			Rate [mm^2/month^2]	95% CI [mm^2/month^2]			Rate [mm^2/month^2]	95% CI [mm^2/month^2]			p-value
MPRAGE	−0.0022	−0.0098	to	0.0054	0.0053	−0.0028	to	0.0134	0.0075	−0.0033	to	0.0183	0.17
synT$_1$-w	−0.0021	−0.0070	to	0.0027	0.0062	0.0010	to	0.0115	0.0084	0.0019	to	0.0149	0.013
Difference	0.0000								0.0009				

CSA cross-sectional area, *MPRAGE* Magnetization Prepared Rapid Acquisition Gradient-Echo image, *synT$_1$-w* synthetic T$_1$-weighted image.

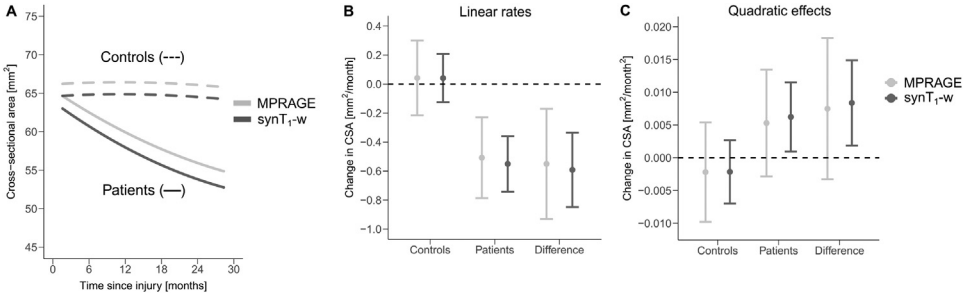

Fig. 4. Change in spinal cord cross-sectional area (CSA) over 2 years for healthy controls (dashed lines) and SCI patients (solid lines) estimated based on MPRAGE (light gray) and synT$_1$-w (dark gray) across C1-C3 (A). Linear rates of controls, SCI patients and the difference between groups estimated from linear mixed effects models (B). Quadratic effects of controls, SCI patients and the difference between groups estimated from linear mixed effects models (C).

Table 5
Cross-sectional cord area averaged across C1-C3 for MPRAGE and synT$_1$-w at baseline and 2-year follow-up estimated from linear mixed effects models.

		Average cross-sectional area											
		Controls				Patients				Patients - Controls			
Time point	Protocol	CSA [mm²]	95% CI [mm²]			CSA [mm²]	95% CI [mm²]			CSA [mm²]	95% CI [mm²]		p-value
Baseline	MPRAGE	66.33	63.40	to	69.27	64.74	61.76	to	67.72	−1.59	−5.76	to 2.58	0.44
	synT$_1$-w	64.81	61.96	to	67.66	63.15	60.23	to	66.08	−1.66	−5.73	to 2.41	0.41
	Difference	−1.52				−1.59				−0.07			
2-year FUP	MPRAGE	65.89	62.02	to	69.76	54.97	50.97	to	58.95	−10.93	−16.45	to −5.42	0.0003
	synT$_1$-w	64.37	60.42	to	68.32	52.90	48.76	to	57.03	−11.48	−17.22	to −5.73	0.0003
	Difference	−1.52				−2.06				−0.54			

CSA cross-sectional cord area, *FUP* follow-up, *MPRAGE* Magnetization Prepared Rapid Acquisition Gradient-Echo image, *synT$_1$-w* synthetic T$_1$-weighted image.

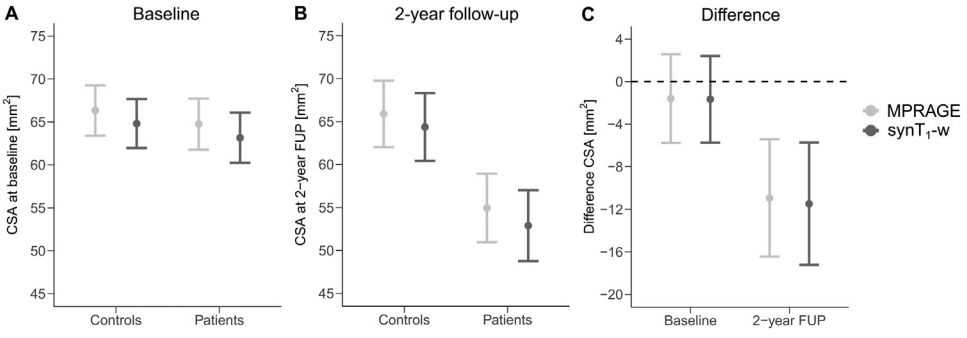

Fig. 5. Average spinal cord cross-sectional area (CSA) at baseline (A) and 2-year follow up (B) for controls and SCI patients, and the difference in CSA between groups (C) estimated from linear mixed effects models. MPRAGE (light gray); synT$_1$-w (dark gray).

images showed high agreement. Moreover, similar estimates of cervical cord atrophy were found with both methods (synT$_1$-w and MPRAGE) in a longitudinal study to track neurodegeneration following SCI.

Conventionally, atrophy of the cervical cord, which is suggested as marker for remote neurodegenerative processes in different diseases such as SCI and multiple sclerosis, is measured on high-resolution T$_1$-w images like 3D MPRAGE (Casserly et al., 2018; Freund et al., 2022; Seif et al., 2019). One major drawback of many MRI study protocols is long acquisition time, which ultimately may impact image quality (Oztek et al., 2020). For reducing acquisition time in extensive MRI study protocols, we calculated synthetic T$_1$-w images based on quantitative maps of PD, R$_1$, and R$_2$* derived from the MPM protocol, using the MPRAGE signal equation. The high test-retest repeatability and high agreement between synT$_1$-w images and MPRAGE images as well as the agreement in atrophy measures following SCI demonstrate that synthetic MRI can replace MPRAGE in clinical studies.

4.1. Intra- and inter-site repeatability

Introduction of new outcome measures to clinical studies require high reliability of the underlying measurements for those outcome measures. Reliability can be assessed by determining the test-retest repeatability. In MRI studies the intra-site repeatability refers to measurements conducted with the same scanner. In this study, the mean intra-site repeatability of synT$_1$-w across C1-C3 was high and ranged between 1.43% and 2.71% for all three cervical levels, which is comparable to the repeatability of CSA measurements based on directly acquired T$_1$-w images (Lukas et al., 2021; Weeda et al., 2019). However, when conducting multi-center studies including acquisition of MR images on different scanners and using different imaging protocols, repeatability of the measurements between the different sites becomes particularly important. Since conventional MRI acquisitions are greatly influenced by the scanner hardware and various protocol parameters, signal intensities may vary considerably between different scanners (Gracien et al., 2020). Quantitative MRI aims at providing quantitative information about specific MRI parameters, which are not anymore influenced by differences between scanners, and thus, should increase repeatability in multi-center studies (Weiskopf et al., 2021). Here, we found that the inter-site CoV of CSA ranged between 2.90% and 5.76%, which is reasonably low. Comparing these results with reliability of directly acquired MRI, the inter-site repeatability of cord segmentation across different MRI systems and protocols was recently addressed in a multi-center study including 42 sites across the world (Cohen-Adad et al., 2021). This study reported inter-site CoV of CSA based on acquired T$_1$-w images (including MPRAGE) separately for different MRI vendors, which ranged between 3.08% and 4.41% being comparable to the results obtained from synT$_1$-w in our study. However, we neither separated the different MRI systems nor averaged the CSA measurements across sev-

eral vertebral levels in our analysis which needs to be considered when comparing these studies (Cohen-Adad et al., 2021; Weeda et al., 2019).

Part of the variability between scan and rescan as well as between different sites might be attributable to remaining variability in the underlying quantitative maps, where recently intra-site repeatability between 2.6 and 7.5%, and inter site-repeatability between 6.5 and 12% for the cervical cord was reported (Seif et al., 2022). However, with improved methods for the quantification of tissue properties, this variability might be reduced in the future.

Comparing the repeatability for vertebral levels separately, there was a trend that lower spinal cord levels showed higher variability, which was expected, given that these regions are located closer to the edge of the field of view.

Overall, the results of intra- and inter-site repeatability of synT$_1$-w segmentations are highly encouraging and support the use of synT$_1$-w for tracking atrophy of the spinal cord in clinical studies. In particular after spinal cord injury, where the effect size of atrophy can be as high as 30% (Freund et al., 2011), synT$_1$-w is expected to allow reliable assessment of CSA atrophy.

4.2. Agreement between CSA from MPRAGE and synT$_1$-w

The validity and applicability of synT$_1$-w images in clinical studies was assessed by directly comparing CSA measurements derived from MPRAGE with those derived from synT$_1$-w in a longitudinal study that involved healthy participants and SCI patients (Azzarito et al., 2020; Freund et al., 2013b; Grabher et al., 2015; Schading et al., 2023; Seif et al., 2018a, 2018b; Ziegler et al., 2018). As the CSA has been proposed as a marker for neurodegeneration in clinical trials (Casserly et al., 2018; Freund et al., 2013a; Kearney et al., 2015; Schmierer and Miquel, 2018; Seif et al., 2019), optimizing acquisition time of study protocols can help to improve patient comfort, data quality and scan costs. However, replacing additional MPRAGE acquisitions by synthetic MRI requires valid measurements of CSA based on synT$_1$-w images. In our study CSA based on synT$_1$-w images showed only a minor bias of −2.5% compared to MPRAGE images in the Bland-Altman analysis.

Considering expected effect sizes of up to −30% (Freund et al., 2011) this difference of −2.5% between both methods is not expected to greatly affect the assessment of neurodegeneration in the cervical cord, given that also the limits of agreement were considerably narrower than this effect size (-8.9 to 3.8%). However, care must be taken when comparing CSA derived from different modalities, particularly when expected effect sizes are considerably smaller (e.g. at early time points post-injury or in different diseases with slower atrophy rates). Therefore, it is recommended to use the same MR protocols in longitudinal studies (Cohen-Adad et al., 2021).

4.3. Tracking SCI-induced cord atrophy using MPRAGE and synT$_1$-w MRI

In order to show that despite this marginal bias of -2.5% valid estimation of cervical cord atrophy in clinical studies is feasible, linear mixed effect models based on MPRAGE and synT$_1$-w images were compared. Overall, a similar difference like in the Bland-Altman analysis between synT$_1$-w and MPRAGE with comparable magnitudes was found in the absolute estimates of CSA when comparing the linear mixed effect models. However, this difference diminished when assessing linear atrophy rates (change/time) and comparisons between groups (SCI patients – controls). This suggests that the absolute difference in segmentation between synT$_1$-w and MPRAGE represents a constant offset with different CSA-intercepts in the linear mixed effect models, while the linear and quadratic estimates of atrophy seem to be less affected. Moreover, both models resulted not only in similar estimates of cord atrophy and differences between healthy controls and SCI patients, but additionally, the variances of the estimates were comparable. This allowed robust estimation of cord atrophy based on synT$_1$-w images despite having a marginal systematic difference compared to MPRAGE. Therefore, synthetic MRI, in particular synT$_1$-w images reconstructed from quantitative maps derived from the MPM protocol (Weiskopf et al., 2013), may be considered as a valid alternative to acquiring additional structural images for morphometry of the cervical cord when MPM data are acquired anyway (Seif et al., 2022). This could help us to reduce acquisition time and to optimize the efficiency of study protocols for improving patient comfort and compliance as well as reduce scanning expenses. Ultimately, it could facilitate the implementation of advanced imaging into clinical MRI protocols.

4.4. Limitations

This study has some limitations. Note that for the optimization of sequence parameters of the synT$_1$-w images we did not conduct a systematic optimization and only considered a certain range of parameters close to the frequently used settings in MPRAGE acquisitions (Tardif et al., 2009). Since the optimum within the predefined range of settings was found at the boundary for several parameters, it is very likely that they do not represent the global optimum. Future studies should focus on systematically optimize these parameters. However, the purpose of this study was not to provide an exhaustive optimization but rather to demonstrate the flexibility and utility of synthetic MRI. For the calculation of the CNR we considered the variance of the signal across the spinal cord instead of measuring only the background noise, as after calculation of the quantitative maps regions outside of the body are not informative about noise anymore. To facilitate segmentation of the spinal cord, we decided to optimize the contrast with respect to the homogeneity of the signal in the spinal cord. Furthermore, the intra- and inter-site repeatability was determined on a small group of five healthy subjects in a narrow age range (32.4 ± 6.0 years). Future studies should extend this analysis to a broader group of patients. Regarding the correction of B_1^+ and B_1^- field inhomogeneities, different approaches were used in both sub-studies. While additional reference scans were acquired in the THS study, a data driven postprocessing correction method (UNICORT) (Weiskopf et al., 2011) was used in the longitudinal study demonstrating the robustness and general applicability of this approach. During the longitudinal study, the scanner was updated to a newer version which involved the change of certain hardware elements including the gradient coils. Since this affected both MPRAGE and synT$_1$-w images, the scanner upgrade is not expected to influence comparisons between these images (Ziegler et al., 2018). Moreover, the statistical models were corrected for the scanner type to account for the scanner upgrade. Healthy controls showed changes in CSA of up to -0.7% over 2 years (difference between baseline and 2-year follow-up), which might be due to aging (Papinutto et al., 2015), natural fluctuations, test-retest variability, or remaining effects of the scanner upgrade. Ultimately, this would limit the ability to detect subtle changes in CSA in diseases where expected effect sizes are rather small such as multiple sclerosis (Prados et al., 2020; Valsasina et al., 2022).

5. Conclusion

This is the first study investigating the feasibility and repeatability of synthetic weighted MRI for tracking neurodegeneration in the cervical cord based on quantitative multi-parameter maps of physical tissue parameters. We demonstrate that macrostructural segmentations of synthetic T$_1$-w images show a high intra- and inter-site repeatability, and only a minor deviation when compared to real MPRAGE images. Most relevant for clinical applications, using these synT$_1$-w images in a longitudinal study to track neurodegeneration within the cervical cord following SCI, the atrophy rates and differences between healthy controls and SCI patients were almost identical to MPRAGE images. Reliable estimates of spinal cord morphology can be obtained from synT$_1$-w derived from MPM images. Thereby the acquisition of a separate MPRAGE scan becomes obsolete and the total acquisition time may be reduced by

approximately 10 min compared to previous comprehensive protocols (Freund et al., 2013b), facilitating the potential application in clinics.

Data availability statement

The authors certify they have documented all data, methods, and materials used to conduct the research presented. Anonymized data pertaining to the research presented will be available by request from investigators.

Funding information

This study was funded by the European Union's Horizon 2020 research and innovation program (No: 681,094), the Swiss State Secretariat for Education, Research and Innovation (SERI) (No: 15.0137), the ERA-NET Neuron (No: 32NE30_173,678), and the Wings for Life Austria (WFL-CH-007/14). SS was supported by a national MD-PhD scholarship from the Swiss National Science Foundation (323,530_207,038), MS received grants from Wings for life charity (No WFL-CH-19/20) and grants from International Foundation for Research in Paraplegia (IRP-158), NW was supported by the Deutsche Forschungsgemeinschaft (DFG, German Research Foundation) – project no. 347,592,254 (WE 5046/4–2) and the Federal Ministry of Education and Research (BMBF) under support code 01ED2210, and PF received a personal grant from the Swiss National Science Foundation (SNF, No. 181,362).

Declaration of Competing Interest

SS reports no conflicts of interest. MS reports no conflicts of interest. TL reports no conflicts of interest. MH reports no conflicts of interest. AC reports no conflicts of interest. NW reports that the Max Planck Institute for Human Cognitive and Brain Sciences has an institutional research agreement with Siemens Healthcare, that he holds a patent on acquisition of MRI data during spoiler gradients (US 10,401,453 B2) and that he was a speaker at an event organized by Siemens Healthcare and was reimbursed for the travel expenses. PF reports no conflicts of interest.

Credit authorship contribution statement

Simon Schading: Formal analysis, Conceptualization, Methodology, Software, Visualization, Writing – original draft. **Maryam Seif:** Investigation, Formal analysis, Conceptualization, Methodology, Data curation, Writing - review & editing. **Tobias Leutritz:** Investigation, Formal analysis, Conceptualization, Data curation, Writing – review & editing. **Markus Hupp:** Investigation, Conceptualization, Writing – review & editing. **Armin Curt:** Conceptualization, Writing – review & editing. **Nikolaus Weiskopf:** Conceptualization, Methodology, Writing – review & editing. **Patrick Freund:** Conceptualization, Methodology, Writing – review & editing, Supervision.

Data availability

Data will be made available on request.

Acknowledgments

The authors thank all participants who gave their time and took part in this study, as well as the staff of the collaborating radiology departments at the clinical research sites for their help in acquiring the MR data and their contribution to the study. These include the departments of radiology at the Clinica Creu Blanca, Barcelona, Spain, at the University Hospital Basel, Basel, Switzerland, at the University Hospital Heidelberg, Heidelberg, Germany, at the Swiss Paraplegic Center, Nottwil, Switzerland, at the Laboratory for Social and Neural Systems Research, Zurich Center for Neuroeconomics, Zurich, Switzerland, and at the University Hospital Balgrist, Zurich, Switzerland.

References

Azzarito, M., Seif, M., Kyathanahally, S., Curt, A., Freund, P., 2020. Tracking the neurodegenerative gradient after spinal cord injury. NeuroimageClin 26, 102221.
Bland, J.M., Altman, D.G., 1986. Statistical methods for assessing agreement between two methods of clinical measurement. Lancet 1, 307–310.
Casserly, C., Seyman, E.E., Alcaide-Leon, P., Guenette, M., Lyons, C., Sankar, S., Svendrovski, A., Baral, S., Oh, J., 2018. Spinal cord atrophy in multiple sclerosis: a systematic review and meta-analysis. J. Neuroimaging 28, 556–586.
Chien, C., Juenger, V., Scheel, M., Brandt, A.U., Paul, F., 2020. Considerations for mean upper cervical cord area implementation in a longitudinal MRI setting: methods, interrater reliability, and MRI quality control. AJNR Am. J. Neuroradiol. 41, 343–350.
Cohen-Adad, J., Alonso-Ortiz, E., Abramovic, M., Arneitz, C., Atcheson, N., Barlow, L., Barry, R.L., Barth, M., Battiston, M., Büchel, C., Budde, M., Callot, V., Combes, A.J.E., De Leener, B., Descoteaux, M., de Sousa, P.L., Dostál, M., Doyon, J., Dvorak, A., Eippert, F., Epperson, K.R., Epperson, K.S., Freund, P., Finsterbusch, J., Foias, A., Fratini, M., Fukunaga, I., Gandini Wheeler-Kingshott, C.A.M., Germani, G., Gilbert, G., Giove, F., Gros, C., Grussu, F., Hagiwara, A., Henry, P.G., Horák, T., Hori, M., Joers, J., Kamiya, K., Karbasforoushan, H., Keřkovský, M., Khatibi, A., Kim, J.W., Kinany, N., Kitzler, H.H., Kolind, S., Kong, Y., Kudlička, P., Kuntke, P., Kurniawan, N.D., Kusmia, S., Labounek, R., Laganà, M.M., Laule, C., Law, C.S., Lenglet, C., Leutritz, T., Liu, Y., Llufriu, S., Mackey, S., Martinez-Heras, E., Mattera, L., Nestrasil, I., O'Grady, K.P., Papinutto, N., Papp, D., Pareto, D., Parrish, T.B., Pichiecchio, A., Prados, F., Rovira, À., Ruitenberg, M.J., Samson, R.S., Savini, G., Seif, M., Seifert, A.C., Smith, A.K., Smith, S.A., Smith, Z.A., Solana, E., Suzuki, Y., Tackley, G., Tinnermann, A., Valošek, J., Van De Ville, D., Yiannakas, M.C., Weber Ii, K.A., Weiskopf, N., Wise, R.G., Wyss, P.O., Xu, J., 2021. Open-access quantitative MRI data of the spinal cord and reproducibility across participants, sites and manufacturers. SciData 8, 219.
De Leener, B., Fonov, V.S., Collins, D.L., Callot, V., Stikov, N., Cohen-Adad, J., 2018. PAM50: unbiased multimodal template of the brainstem and spinal cord aligned with the ICBM152 space. Neuroimage 165, 170–179.
De Leener, B., Kadoury, S., Cohen-Adad, J., 2014. Robust, accurate and fast automatic segmentation of the spinal cord. Neuroimage 98, 528–536.
De Leener, B., Lévy, S., Dupont, S.M., Fonov, V.S., Stikov, N., Louis Collins, D., Callot, V., Cohen-Adad, J., 2017. SCT: spinal Cord Toolbox, an open-source software for processing spinal cord MRI data. Neuroimage 145, 24–43.
Deichmann, R., Good, C., Josephs, O., Ashburner, J., Turner, R., 2000. Optimization of 3D MP-RAGE sequence for structural brain imaging. Neuroimage 12, 112–127.
Freund, P., Curt, A., Friston, K., Thompson, A., 2013a. Tracking changes following spinal cord injury: insights from neuroimaging. Neuroscientist 19, 116–128.
Freund, P., Papinutto, N., Bischof, A., Azzarito, M., Kirkish, G., Ashburner, J., Thompson, A., Hauser, S.L., Henry, R.G., 2022. Simultaneous assessment of regional distributions of atrophy across the neuraxis in MS patients. NeuroimageClin 34, 102985.
Freund, P., Weiskopf, N., Ashburner, J., Wolf, K., Sutter, R., Altmann, D.R., Friston, K., Thompson, A., Curt, A., 2013b. MRI investigation of the sensorimotor cortex and the corticospinal tract after acute spinal cord injury: a prospective longitudinal study. Lancet Neurol 12, 873–881.
Freund, P., Weiskopf, N., Ward, N.S., Hutton, C., Gall, A., Ciccarelli, O., Craggs, M., Friston, K., Thompson, A.J., 2011. Disability, atrophy and cortical reorganization following spinal cord injury. Brain 134, 1610–1622.
Freund, P.A., Dalton, C., Wheeler-Kingshott, C.A., Glensman, J., Bradbury, D., Thompson, A.J., Weiskopf, N., 2010. Method for simultaneous voxel-based morphometry of the brain and cervical spinal cord area measurements using 3D-MDEFT. J. Magn. Reson. Imaging 32, 1242–1247.
Grabher, P., Callaghan, M.F., Ashburner, J., Weiskopf, N., Thompson, A.J., Curt, A., Freund, P., 2015. Tracking sensory system atrophy and outcome prediction in spinal cord injury. Ann. Neurol. 78, 751–761.
Gracien, R.M., Maiworm, M., Brüche, N., Shrestha, M., Nöth, U., Hattingen, E., Wagner, M., Deichmann, R., 2020. How stable is quantitative MRI? – assessment of intra- and inter-scanner-model reproducibility using identical acquisition sequences and data analysis programs. Neuroimage 207, 116364.
Gracien, R.M., van Wijnen, A., Maiworm, M., Petrov, F., Merkel, N., Paule, E., Steinmetz, H., Knake, S., Rosenow, F., Wagner, M., Deichmann, R., 2019. Improved synthetic T1-weighted images for cerebral tissue segmentation in neurological diseases. Magn. Reson. Imaging 61, 158–166.
Granberg, T., Uppman, M., Hashim, F., Cananau, C., Nordin, L.E., Shams, S., Berglund, J., Forslin, Y., Aspelin, P., Fredrikson, S., Kristoffersen-Wiberg, M., 2016. Clinical feasibility of synthetic mri in multiple sclerosis: a diagnostic and volumetric validation study. AJNR Am. J. Neuroradiol. 37, 1023–1029.
Gros, C., De Leener, B., Badji, A., Maranzano, J., Eden, D., Dupont, S.M., Talbott, J., Zhuoquiong, R., Liu, Y., Granberg, T., Ouellette, R., Tachibana, Y., Hori, M., Kamiya, K., Chougar, L., Stawiarz, L., Hillert, J., Bannier, E., Kerbrat, A., Edan, G., Labauge, P., Callot, V., Pelletier, J., Audoin, B., Rasoanandrianina, H., Brisset, J.C., Valsasina, P., Rocca, M.A., Filippi, M., Bakshi, R., Tauhid, S., Prados, F., Yiannakas, M., Kearney, H., Ciccarelli, O., Smith, S., Treaba, C.A., Mainero, C., Lefeuvre, J., Reich, D.S., Nair, G., Auclair, V., McLaren, D.G., Martin, A.R., Fehlings, M.G., Vahdat, S., Khatibi, A., Doyon, J., Shepherd, T., Charlson, E., Narayanan, S., Cohen-Adad, J., 2019. Automatic segmentation of the spinal cord and intramedullary multiple sclerosis lesions with convolutional neural networks. Neuroimage 184, 901–915.
Helms, G., Dathe, H., Dechent, P., 2008. Quantitative FLASH MRI at 3T using a rational approximation of the Ernst equation. Magn. Reson. Med. 59, 667–672.
Kearney, H., Miller, D.H., Ciccarelli, O., 2015. Spinal cord MRI in multiple sclerosis–diagnostic, prognostic and clinical value. Nat. Rev. Neurol. 11, 327–338.
Leutritz, T., Seif, M., Helms, G., Samson, R.S., Curt, A., Freund, P., Weiskopf, N., 2020. Multiparameter mapping of relaxation (R1, R2*), proton density and magnetization

transfer saturation at 3 T: a multicenter dual-vendor reproducibility and repeatability study. Hum. Brain Mapp. 41, 4232–4247.

Lukas, C., Bellenberg, B., Prados, F., Valsasina, P., Parmar, K., Brouwer, I., Pareto, D., Rovira, À., Sastre-Garriga, J., Gandini Wheeler-Kingshott, C.A.M., Kappos, L., Rocca, M.A., Filippi, M., Yiannakas, M., Barkhof, F., Vrenken, H., 2021. Quantification of cervical cord cross-sectional area: which acquisition, vertebra level, and analysis software? a multicenter repeatability study on a traveling healthy volunteer. FrontNeurol 12, 693333.

Lundell, H., Barthelemy, D., Skimminge, A., Dyrby, T.B., Biering-Sørensen, F., Nielsen, J.B., 2011. Independent spinal cord atrophy measures correlate to motor and sensory deficits in individuals with spinal cord injury. Spinal Cord 49, 70–75.

Nöth, U., Hattingen, E., Bähr, O., Tichy, J., Deichmann, R., 2015. Improved visibility of brain tumors in synthetic MP-RAGE anatomies with pure T1 weighting. NMR Biomed. 28, 818–830.

Oztek, M.A., Brunnquell, C.L., Hoff, M.N., Boulter, D.J., Mossa-Basha, M., Beauchamp, L.H., Haynor, D.L., Nguyen, X.V., 2020. Practical Considerations for Radiologists in Implementing a Patient-friendly MRI Experience. Top. Magn. Reson. Imaging. 29, 181–186.

Papinutto, N., Asteggiano, C., Bischof, A., Gundel, T.J., Caverzasi, E., Stern, W.A., Bastianello, S., Hauser, S.L., Henry, R.G., 2020. Intersubject variability and normalization strategies for spinal cord total cross-sectional and gray matter areas. J. Neuroimaging 30, 110–118.

Papinutto, N., Schlaeger, R., Panara, V., Zhu, A.H., Caverzasi, E., Stern, W.A., Hauser, S.L., Henry, R.G., 2015. Age, gender and normalization covariates for spinal cord gray matter and total cross-sectional areas at cervical and thoracic levels: a 2D phase sensitive inversion recovery imaging study. PLoS One 10, e0118576.

Prados, F., Moccia, M., Johnson, A., Yiannakas, M., Grussu, F., Cardoso, M.J., Ciccarelli, O., Ourselin, S., Barkhof, F., Wheeler-Kingshott, C., 2020. Generalised boundary shift integral for longitudinal assessment of spinal cord atrophy. Neuroimage 209, 116489.

Schading, S., David, G., Max Emmenegger, T., Achim, C., Thompson, A., Weiskopf, N., Curt, A., Freund, P., 2023. Dynamics of progressive degeneration of major spinal pathways following spinal cord injury: a longitudinal study. NeuroimageClin 37, 103339.

Schmierer, K., Miquel, M.E., 2018. Magnetic resonance imaging correlates of neuro-axonal pathology in the MS spinal cord. Brain Pathol. 28, 765–772.

Seif, M., Curt, A., Thompson, A.J., Grabher, P., Weiskopf, N., Freund, P., 2018a. Quantitative MRI of rostral spinal cord and brain regions is predictive of functional recovery in acute spinal cord injury. NeuroimageClin. 20, 556–563.

Seif, M., Gandini Wheeler-Kingshott, C.A., Cohen-Adad, J., Flanders, A.E., Freund, P., 2019. Guidelines for the conduct of clinical trials in spinal cord injury: neuroimaging biomarkers. Spinal Cord 57, 717–728.

Seif, M., Leutritz, T., Schading, S., Emmengger, T., Curt, A., Weiskopf, N., Freund, P., 2022. Reliability of multi-parameter mapping (MPM) in the cervical cord: a multi-center multi-vendor quantitative MRI study. Neuroimage 264, 119751.

Seif, M., Ziegler, G., Freund, P., 2018b. Progressive ventricles enlargement and cerebrospinal fluid volume increases as a marker of neurodegeneration in patients with spinal cord injury: a longitudinal magnetic resonance imaging study. J. Neurotrauma 35, 2941–2946.

Tabelow, K., Balteau, E., Ashburner, J., Callaghan, M.F., Draganski, B., Helms, G., Kherif, F., Leutritz, T., Lutti, A., Phillips, C., Reimer, E., Ruthotto, L., Seif, M., Weiskopf, N., Ziegler, G., Mohammadi, S., 2019. hMRI - A toolbox for quantitative MRI in neuroscience and clinical research. Neuroimage 194, 191–210.

Tanenbaum, L.N., Tsiouris, A.J., Johnson, A.N., Naidich, T.P., DeLano, M.C., Melhem, E.R., Quarterman, P., Parameswaran, S.X., Shankaranarayanan, A., Goyen, M., Field, A.S., 2017. Synthetic MRI for Clinical Neuroimaging: results of the Magnetic Resonance Image Compilation (MAGiC) Prospective, Multicenter, Multireader Trial. AJNR Am. J. Neuroradiol. 38, 1103–1110.

Tardif, C.L., Collins, D.L., Pike, G.B., 2009. Sensitivity of voxel-based morphometry analysis to choice of imaging protocol at 3 T. Neuroimage 44, 827–838.

Valsasina, P., Horsfield, M.A., Meani, A., Gobbi, C., Gallo, A., Rocca, M.A., Filippi, M., 2022. Improved assessment of longitudinal spinal cord atrophy in multiple sclerosis using a registration-based approach: relevance for clinical studies. J. Magn. Reson. Imaging 55, 1559–1568.

Weeda, M.M., Middelkoop, S.M., Steenwijk, M.D., Daams, M., Amiri, H., Brouwer, I., Killestein, J., Uitdehaag, B.M.J., Dekker, I., Lukas, C., Bellenberg, B., Barkhof, F., Pouwels, P.J.W., Vrenken, H., 2019. Validation of mean upper cervical cord area (MUCCA) measurement techniques in multiple sclerosis (MS): high reproducibility and robustness to lesions, but large software and scanner effects. Neuroimage. Clin. 24, 101962.

Weiskopf, N., Callaghan, M.F., Josephs, O., Lutti, A., Mohammadi, S., 2014. Estimating the apparent transverse relaxation time (R2(*)) from images with different contrasts (ESTATICS) reduces motion artifacts. Front. Neurosci. 8, 278 -278.

Weiskopf, N., Edwards, L.J., Helms, G., Mohammadi, S., Kirilina, E., 2021. Quantitative magnetic resonance imaging of brain anatomy and in vivo histology. Nat. Rev. Phys. 3, 570–588.

Weiskopf, N., Lutti, A., Helms, G., Novak, M., Ashburner, J., Hutton, C., 2011. Unified segmentation based correction of R1 brain maps for RF transmit field inhomogeneities (UNICORT). Neuroimage 54, 2116–2124.

Weiskopf, N., Suckling, J., Williams, G., Correia, M.M., Inkster, B., Tait, R., Ooi, C., Bullmore, E.T., Lutti, A., 2013. Quantitative multi-parameter mapping of R1, PD(*), MT, and R2(*) at 3T: a multi-center validation. Front. Neurosci. 7, 95.

Ziegler, G., Grabher, P., Thompson, A., Altmann, D., Hupp, M., Ashburner, J., Friston, K., Weiskopf, N., Curt, A., Freund, P., 2018. Progressive neurodegeneration following spinal cord injury: implications for clinical trials. Neurology 90, e1257–e1266.